The Design and Implementation of a Magnetorheological Silicone Composite State-Switched Absorber

A Thesis
Presented to
The Academic Faculty

by

Anne-Marie Albanese Lerner

In Partial Fulfillment
of the Requirements for the Degree
Master of Science

School of Mechanical Engineering
Georgia Institute of Technology
August 2005

The Design and Implementation of a Magnetorheological Silicone Composite State-Switched Absorber

Approved by:

Dr. Ken Cunefare
School of Mechanical Engineering
Georgia Institute of Technology

Dr. Christopher Lynch
School of Mechanical Engineering
Georgia Institute of Technology

Dr. Nader Sadegh
School of Mechanical Engineering
Georgia Institute of Technology

Date Approved: May 24 , 2005

For Dan,

who lovingly and patiently encouraged me to pursue my dreams.

ACKNOWLEDGEMENTS

I want to thank Dr. Ken Cunefare, without whom this research would not be possible. I would also like to thank my committee members, Dr. Chris Lynch, and Dr. Nader Sadegh, for their contributions to my studies and research. My labmates, especially Mark Holdhusen, have provided invaluable insights and advice that helped me along the way.

TABLE OF CONTENTS

LIST OF FIGURES

SUMMARY

Tuned vibration absorbers (TVAs) are spring-mass-damper devices used to minimize energy in a vibrating body. TVAs decrease in efficiency when the vibrating body is subjected to variable, broadband, or random excitation. A state-switched absorber (SSA) can be used in these variable, broadband, or random excitation cases to more effectively reduce excitation. An SSA is a mass-spring-damper where one or more of these elements can instantaneously and discretely change. An SSA was designed, built and tested to fit the specifications for TVAs found on ATR 72 and 42 airplane fuselages. A magnetorheological elastomer (MRE), an elastomer with imbedded iron particles, was selected as a variable spring. Flux lines concentrated through all MREs in absorber configurations. MREs containing 35% iron by volume yielded the largest frequency shift. A 35% MRE based absorber had a frequency range of 45-183 Hz, which corresponds to a 360% frequency increase. Transient absorber behavior was observed by recording rise and drop times to step field intensity changes.The 35% MRE absorber yielded a 0.20 second rise time and a 0.03 second drop time. Future work will determine whether a modified input signal can generate an appropriate transient response.

CHAPTER I

INTRODUCTION

Tuned vibration absorbers (TVAs) are mass-spring-damper systems designed to reduce vibration of a base mass to which the TVA is attached [13]. While highly effective at controlling single-frequency excitation, TVA performance must be compromised to suppress multiharmonic, broadband, or variable-frequency excitation [25]. For these excitations, adaptive elements can be employed as an element of a semi-active absorber (SA), active vibration absorber (AVA), or adaptive tunable vibration absorber (ATVA) to more effectively suppress vibration. The purpose of this work was to identify and develop an adaptive material as a tunable spring and investigate its mechanical properties in vibration absorber configurations similar in characteristics to those used on ATR 72 and 42 airplanes.

Tuned vibration absorbers have been used to suppress vibration on vehicles, machinery, and equipment, and implemented in multiple and single degree of freedom systems, and continuous systems [9]. TVAs minimize base energy if the absorber's impedance is maximized at the operational frequency of interest. However, if the operational frequency varies with time, or if the excitation is broadband in nature, design compromises must be made to ensure that base excitation does not exceed set levels for the entire frequency range of interest.

The design compromises made to implement TVAs for broadband or variable excitation control may lead to unacceptable attenuation performance [30]. For these types of excitation, AVAs, ATVAs, or SAs may be implemented. AVAs, ATVAs, and SAs are similar in structure to TVAs, in that they are mass-spring-damper systems. AVAs, ATVAs and SAs differ from TVAs in that one or more of their elements are allowed to vary controllably to an external input, and are hence called an adaptive element.

AVAs are vibration suppression devices that contain at least one adaptive element, and the adaptive element is allowed to continuously change. AVAs are best suited for

applications where TVA devices do not guarantee stability due to constantly changing input excitation [23], such as to helicopter rotors, flexible aerospace vehicle bending vibration, or when TVAs can not control vibration within acceptable limits, such as fighter pilot motion within aircraft [22]. AVAs have also been shown to outperform TVAs when responding to broadband excitation [26]. Although AVAs are effective vibration suppression tools, they carry the risk of inducing instability if controlled improperly [2].

ATVAs are similar to AVAs in that ATVAs are vibration suppression devices containing at least one adaptive element. The difference between an AVA and an ATVA is that the adaptive element in an ATVA is allowed to change very slowly with respect to the excitation frequency. While AVAs are implemented for broadband and rapidly changing excitations, ATVAs are used primarily for systems that are not well defined [30]. An ATVA allows its adaptive element to change only slowly over time, until an optimal parameter has been found. Once the optimal parameter has been found, the device will stay in that state and behave as a TVA. The quasi-static nature of these changes means that the possibility of instability is small.

While ATVAs contain an adaptive element that changes slowly over time, adaptive elements in SAs are permitted to only change at discrete instants to discrete property states. Although SAs can add energy at discrete instants, the risk of leading to instability is less than that of AVAs. This means that SAs can be significantly more robust than AVAs [22]. Despite these advantages, SAs are not appropriate for every application. Their utilization is limited to those applications where TVAs do not achieve satisfactory performance, but where AVAs are not absolutely necessary.

One type of SA is the state-switched absorber, or SSA. An SSA is an adaptive vibration absorber that contains an adaptive spring. This spring is permitted to switch states only at zero-strain conditions, so that the system does not receive mechanical shocks. SSAs have been found to equal or improve upon optimal TVA performance for multi-tone vibration excitation [5], [6].

AVAs, SAs, SSAs, and ATVAs are similar in that they each possess adaptive elements, and these adaptive elements must behave suitably for each type of device. An adaptive

element must operate in the appropriate frequency range, exhibit a sufficiently large operational frequency range, and respond to changing input parameters in a timely manner. The difference between each of these devices is simply in the control scheme that causes the adaptive element to change. The objective of the work presented here is to develop a tunable spring for use in an SSA vibration absorber device; however, the control of the SSA is beyond the scope of this work.

1.1 Objectives

Although device control is beyond the scope of this work, the purpose of this work is to develop an adaptive material suitable for use as a tunable spring and to characterize its properties in a vibration absorber device that could serve as an AVA, SA, or ATVA, but particularly for use within an SSA. The vibration absorber device was to be an active analog to the Barry Controls TVA found on ATR 72 and 42 airplane fuselages. To be an active analog, the vibration absorber device developed here would have to occupy roughly the same volume, be of equivalent mass, and operate in the same frequency range. Furthermore, its response to a signal for a change in stiffness must be measured to determine in what type of vibration absorber it could be used. In quantitative terms, the vibration absorber device must consist of all length scales less than 5 cm, weigh less than 100 g, and be able to operate below 100 Hz. Since this device was designed for use as an SSA, the adaptive element needed to have variable stiffness capabilities. Ideal materials for SSA applications also have Q-values in a range of 0.84 to 1.68 [20]. The size, mass, and operational objectives were used to determine which of the currently available adaptive elements were most appropriate for this work.

1.2 Adaptive Elements

Given the design constraints, the adaptive element must be chosen carefully to adhere to the design specifications. Piezoceramics, electrorheological (ER) fluids and elastomers, and magnetorheological (MR) fluids, foams, and elastomers are all materials whose rheologies are known to change in the presence of an external input. The properties of each of these

materials were first considered before designing the vibration absorber.

1.2.1 Piezoceramics

One type of adaptive element is a piezoceramic. Piezoceramics are ceramic composites that deform when voltage is applied, and produce voltage when a deformation is applied. They have been used in large space structures [4], [7], aircraft fuselages [10], and rotationally periodic structure [31] vibration control applications. Piezoceramics are by nature quite stiff, but can be used in sub-100 Hz applications either by employing large masses or when implementing a technique called displacement amplification. Displacement amplification is a process by which a piezoceramic is attached to a much longer structure, causing a much larger displacement and lower natural frequencies to be generated [10]. A capacitive shunt allows stiffness modification without affecting the damping, whereas a resistive shunt allows both damping and natural frequency retuning. As much as a 5% frequency shift can be achieved to "fine tune" an absorber to its tuning frequency using these shunting techniques [7]. While displacement amplification techniques have broadened piezoceramics' operational bandwidth, a piezoceramic device cannot achieve both the size and operational frequency requirements necessary for this work.

1.2.2 Electrorheological Fluids and Elastomers

While a piezoceramic deforms in the presence of an electric field, an electrorheological (ER) fluid experiences an increased yield stress in the presence of an electric field. An ER fluid consists of electrically conductive particles suspended in oil or other liquid. ER fluids are most effective when the suspending liquid is anhydrous, or not electrically-conductive [15]. The advantage to an ER fluid is that the necessary current and power requirements are very low, making an ER fluid controllable with a simple battery. One disadvantage with ER fluids is that they have low yield stresses, on the order of only several kPa, and despite low current and power requirements, they require high electrical fields of several kiloVolts/mm.

An ER fluid works as an active element by increasing its yield stress with increasing electric field. Although they are normally used in low-force actuators, they can become part of high-force actuators if the ER fluid is placed in a series of concentric circles of alternating

charges [14]. ER fluids are ideally suited for switchable damper applications, but have not yet been commercially implemented due to the aforementioned disadvantages.

ER elastomers are similar to ER fluids in that they contain electrically conducting particles suspended in an anhydrous base material, but the base material in ER elastomers is elastomeric. This means that unlike the particles in ER fluids, these particles are not free to move, and will not fall out of suspension. ER elastomers can be used as variable springs [27]. ER elastomers have not been heavily commercialized, as ER elastomers must also be subjected to large electric fields in order to exhibit a stiffness change.

1.2.3 Magnetorheological Fluids

Ferrofluids and MR fluids both consist of magnetically permeable particles dispersed throughout either a polar or nonpolar fluid. Ferrofluids and MR fluids have been used over ER fluids because the devices do not require large voltages. Ferrofluids typically consist of much smaller particles and have lower particle concentrations than magnetorheological fluids.

MR fluids were first developed in 1951 by J. Rabinow [28], who was inspired by ER fluid development. The magnetic particles are typically 10 nm to 10 mm in size [16], in volume concentrations of 0.1-0.5. The volume fraction is chosen to best decrease sedimentation velocity and increase magnetorheological effects without increasing the zero-field velocity to an unacceptable level.

MR fluid behavior has been studied extensively in recent years. In the absence of a magnetic field, the fluid is generally modeled as a Newtonian fluid. If a particle is partially saturated, it is classified as an intermediate field, whereas fully saturated particles are called high fields. For intermediate fields, $G' \propto \phi M_s H_0$, where G' is the shear modulus of the composite fluid, ϕ is the particle volume fraction, M_s is the saturation magnetization, and H_0 is the applied magnetic field. If the fluid is in the presence of a high magnetic field, then $G' \propto \phi M_s^2$ [17].

Both MR fluids and ferrofluids have been used in a number of applications. Ferrofluids have found use in rotary seal, magnetic bearing, motor damper, and loudspeaker voice coil damper applications [16]. MR fluids, on the other hand, have been used in seal mounts,

as variable damping brakes for exercise equipment, and in engine mount applications [16]. Since both ferrofluids and MR fluids are used for variable damping applications, these materials were deemed inappropriate for this work's design objectives.

1.2.4 Magnetorheological Elastomers

An MR elastomer consists of iron particles dispersed through an elastomeric host. While the iron particles in MR fluids are allowed to float and can thus fall out of suspension, the elastomeric matrix of an MR elastomer keeps the iron particles permanently in suspension. An MR elastomer can be characterized as a Bingham plastic always operating in the preyield regime. The primary difference between an MR fluid and elastomer in switching mechanics is that an MR elastomer's stiffness changes, whereas the MR fluid switches from pre- to post-yield stress regimes, which causes a net damping change. Although MR elastomers have not been commercialized as heavily as MR fluids, the research seems to favor MR elastomer in a variable stiffness suspension bushing application [18], [32].

Before the magnetorheological properties associated with an iron-doped elastomer can be discussed, the effect of particulate matter on elastomeric properties must be considered. Eugene Guth characterized the behavior of composites doped with filler particles as increasing the Young's and shear stiffness moduli [19]. Guth theorized that

$$E' = E_0 \left(1 + 2.5\phi + 14.1\phi^2\right), \tag{1.1}$$

where E_0 is the unfilled elastomer modulus ϕ is the particulate volume fraction. This relationship between ϕ and E' has been experimentally verified [24].

If the particles are magnetically conducting, the particulate volume fraction affects not only the zero-field stiffness modulus, but also affects the amount of increased stiffness in the presence of a magnetic field. As much as a 50% increase in stiffness could be generated if the iron content was 27% by volume [8]. Not only is the particle quantity in the elastomer important, but its orientation within the elastomer also plays a prominent role. The presence of iron will cause the stiffness to increase, but if these iron particles are aligned in chains, the stiffness increase will be about 20% larger [3]. The particles will align in chains if the

elastomer is cured in the presence of a magnetic field; this has become a common practice in MR elastomer development.

Although the zero-field elastomer properties have been well understood for some time, a recent focus has been on the magnetic mechanisms that induce a stiffness increase. First attempts at modeling magnetic behavior assumed the iron particles to be point dipoles in a magnetic field and that small strain amplitudes were excited. These assumptions lead to the finding that shear modulus $G \propto H^2$ [29], [21], where H is the magnetic field strength. This theory was experimentally confirmed in 1999 [8], and an estimate for the maximum stiffness shift possible was estimated to be

$$\frac{\Delta G_{\max}}{G\left(0\right)} = \frac{1.913\phi}{G_0}, \tag{1.2}$$

where $G\left(0\right)$ is the zero-field shear modulus of the filled elastomer, G_0 is the shear modulus of the unfilled elastomeric host, and ϕ is the fraction of ferromagnetic particles. This finding is restricted, however, to the case where there is no deformation in the direction of the iron chains. The squared relationship between the magnetic field and shear stress did not hold for all cases. Ginder found a sub-square relationship between G and H for nonsaturated iron particles [16]. Zhou stated further that the magnetic dipole assumption does not hold true for magnetic fields lower than 0.8 Tesla, and that local magnetic saturation in particles must be included for these cases [33].

The mathematical analyses for stiffness shifting have been studied only for the case of shear stiffness and excitation. Little experimentation and no theoretical development have been conducted on MR elastomers in squeeze or longitudinal mode configurations shown in Figure 1.1. However, a 300% compression modulus increase has been reported in longitudinal setups [12].

Since these materials can have low stiffnesses and can operate as variable springs, magnetorheological elastomers (MREs) were selected for use in this experimental work. While piezoceramics also experience stiffness changes in response to a voltage gradient, MREs can have very low stiffnesses as compared to piezoceramics. Furthermore, MREs require very little power.

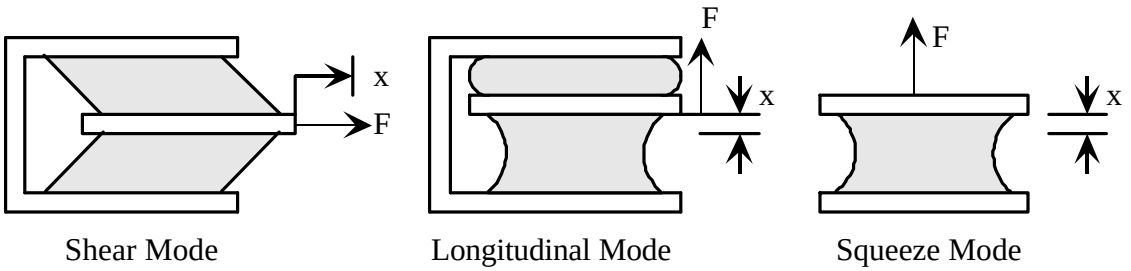

Figure 1.1: Shear, longitudinal, and squeeze mode devices and direction of excitation.

The MRE characteristics described in this section are considered in the Device Design and Construction chapter to develop three vibration absorbers, similar in appearance to the vibration absorbers in Figure 1.1. MREs were sandwiched in between iron pieces to form vibration absorbers, and then vibration absorber performance was measured. In this way, MRE characteristics were analyzed as a function of the vibration absorber's characteristics. Each of these vibration absorbers satisfies the design criteria established in the Objectives section. A general experimental procedure was created that required minimal setup change to examine not only the effect of MRE ferromagnetic particulate concentration on natural frequency change, and hence stiffness change, but also to examine transient properties associated with a change in magnetic field. The experimental setup, the results of experimentation, and an analysis of the results' implications are presented in the Experimental Setup, Results, and Discussion chapter. The Conclusions chapter summarizes the findings from this work.

CHAPTER II

DEVICE DESIGN AND CONSTRUCTION

Magnetorheological elastomers were chosen to be the adaptive element for three vibration absorber designs. One vibration absorber would be operated in shear, one would be operated in the longitudinal direction, and one would operate in squeeze-mode. These devices will be referred to simply as shear, longitudinal, and squeeze devices.

Each device was designed so that a magnetic field of sufficient strength could be generated and travel through MREs on each device, and yet still adhere to the specifications set forth in the Objectives section. A mold was built to cure MREs, and a MRE production procedure was established. Device construction procedures were also established. The remainder of this chapter focuses on the device design, mold design, and device construction procedures.

2.1 Device Design

Three vibration absorbers were designed to operate in longitudinal, shear, and squeeze mode. These devices were specified to weigh less than 100 g, be no longer than 5 cm in any direction, and to operate at frequencies less than 100 Hz. These devices also needed to be able to convey sufficient magnetic fields through the MREs in order to achieve a frequency shift. This section presents the variables and variable interactions between different criteria considered that enabled three devices to be designed. Since the design procedure was identical for each device, only the design procedure for the squeeze mode device will be presented.

Figure 2.1 shows a basic squeeze mode design shape that was used to begin the design process, along with the dimensional variables involved. Each device consisted of five components: an absorber mass, a base mass, two MREs, and a coil of magnet wire. The magnet wire coil was wound around the absorber mass. For initial design purposes, the absorber

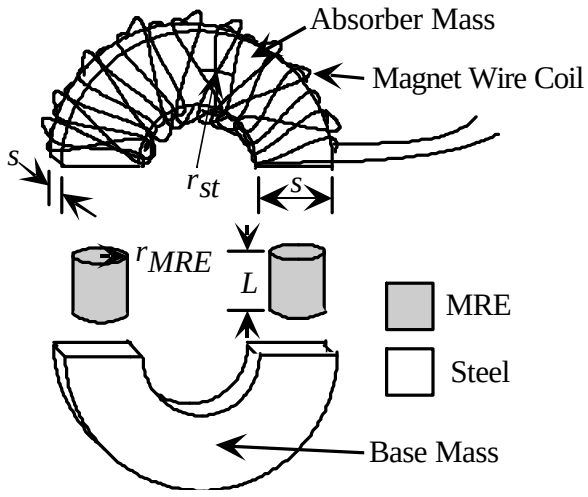

Figure 2.1: A preliminary squeeze mode device shape and variable parameters.

mass was assumed to weigh 50 g. An elastomeric silicone gel was chosen for the MRE host matrix such that $E \approx 2.5 \times 10^4$ Pa. This was done so that, given the design constraints, a net natural frequency of $\omega_n \approx 50$ Hz could be achieved.

Figure 2.1 shows five physical parameters used to design the device; the steel had a square cross-sectional area of length s and curvature of radius r_{st}. Each elastomer was cylindrically shaped with radius r_{MRE} and length L. Wire was wound around the absorber mass to create a wire coil capable of generating a magnetic field; the variables considered when building the wire coil was the number of turns N, and the gage of the wire.

Figure 2.2 shows the magnetic flux lines and their implied density as it crosses through steel, an MRE, and back through steel. In order for a design to be successful, a magnetic field capable of magnetically saturating iron particles must be generated through the MRE. In order to magnetically saturate iron particles, the flux density through the iron particles in the MRE must be 21 kG. Assuming that the iron particulate concentration in the MRE is $\phi = 0.3$, and that all flux density travels through the particles, and none of the magnetic field will go through the pure elastomer, the net magnetic flux density through the MRE is found to be $B_{MRE} = 6$ kG.

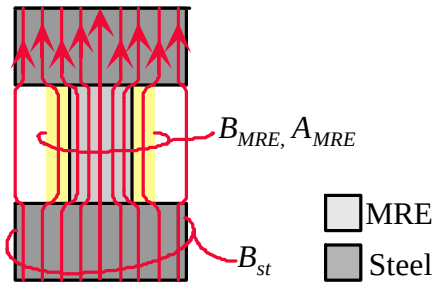

Figure 2.2: Flux density through steel and through and MRE.

The relationship between the MRE flux density and the flux density through the steel is

$$B_{MRE} = \frac{B_{st} \cdot A_{st}}{A'_{MRE}}, \tag{2.1}$$

where A_{st} is the steel mass face area and A'_{MRE} is the effective pole area, which accounts for fringing effects [1]. The effective pole area consists of the MRE and the yellow area surrounding the MRE in Figure 2.2. The effective pole area was found by

$$A'_{MRE} = \pi \left(r_{MRE} + \frac{1}{2} L \right)^2, \tag{2.2}$$

where r_{MRE} is the radius of the MRE and L is the length of the MRE. In order to achieve the desired $B_{MRE} = 6$ kG, a flux density must be present throughout the steel bases. The flux density through the steel base, B_{st}, was generated by creating a wire coil featuring N turns of wire carrying current, I, in Amperes. This coil created magnetic fields throughout the device according to Ampere's circuit law such that

$$NI = \oint H \cdot dl, \tag{2.3}$$

where H is the magnetic field at any point in a magnetic circuit, and dl is the differential length at a given point in a circuit. The magnetic field, H, is related to magnetic flux density, B, in a material-dependent, nonlinear fashion. For the devices considered in this research, Equation 2.3 can be simplified to

$$NI = 2 \left(L H_{MRE} + \pi r_{st} H_{st} \right), \tag{2.4}$$

where L is the MRE length, H_{MRE} is the magnetic field through the MRE, r_{st} is the average radius of the steel according to Figure 2.3, and H_{st} is the magnetic field through the base and absorber masses.

In addition to satisfying the magnetic requirements, the physical constraints must also be satisfied. The physical constraints included the physical limitation of any length scale to less than 5 cm, a total mass of less than 100 g, and the device's natural frequency less than 100 Hz. Since the longest length scale may be described by

$$L_{longest} = 2r_{st} + s + L, \tag{2.5}$$

where s is the depth of the base and absorber masses, the length scale requirements were satisfied by ensuring that Equation 2.5 never exceeds 5 cm. The total mass, m_t, was found to be

$$\begin{aligned} m_t &= \pi \left\{ \rho_{st} \left[\left(r_{st} + \frac{1}{2}s \right)^2 - \left(r_{st} - \frac{1}{2}s \right)^2 \right] s + \rho_{MRE} r^2 L \right\} + M_{wire}, \\ &= \pi \left(2\rho_{st} \left(r_{st}^2 - \frac{1}{4}s^2 \right) s + \rho_{MRE} r^2 L \right) + M_{wire} < 100g \end{aligned} \tag{2.6}$$

where M_{wire} is the mass of the magnet wire, ρ_{st} is the density of steel, and ρ_{MRE} is the MRE composite density. The composite density was determined to be $\rho_{MRE} = \phi\rho_{st} + (1-\phi)\,\rho_e$, where ϕ is the volume fraction of iron, assumed to be $\phi = 27\%$ for design purposes, and ρ_e is the unfilled elastomer density. The natural frequency, in the absence of a magnetic field, is

$$\omega_n = \sqrt{\frac{2E' A_{MRE}}{LM_{abs}}}, \tag{2.7}$$

where E' was estimated with a ϕ value of 0.27. Substituting Equations 2.2 and 1.1, and knowing that $M_{abs} = \rho_{st} s \left(r_{st}^2 - \frac{1}{4}s^2 \right)$ yields a natural frequency such that

$$\begin{aligned} \omega_n &\approx \sqrt{\frac{2\left(2.70E_0\right)\left[\pi\left(r_{MRE} + \frac{1}{2}L\right)^2\right]}{L\left[\rho_{st}s\left(r_{st}^2 - \frac{1}{4}s^2\right) + M_{wire}\right]}} \\ &= \left(r_{MRE} + \frac{1}{2}L \right) \sqrt{\frac{5.40E_0}{L\left[\rho_{st}s\left(r_{st}^2 - \frac{1}{4}s^2\right) + M_{wire}\right]}} < 200\pi. \end{aligned} \tag{2.8}$$

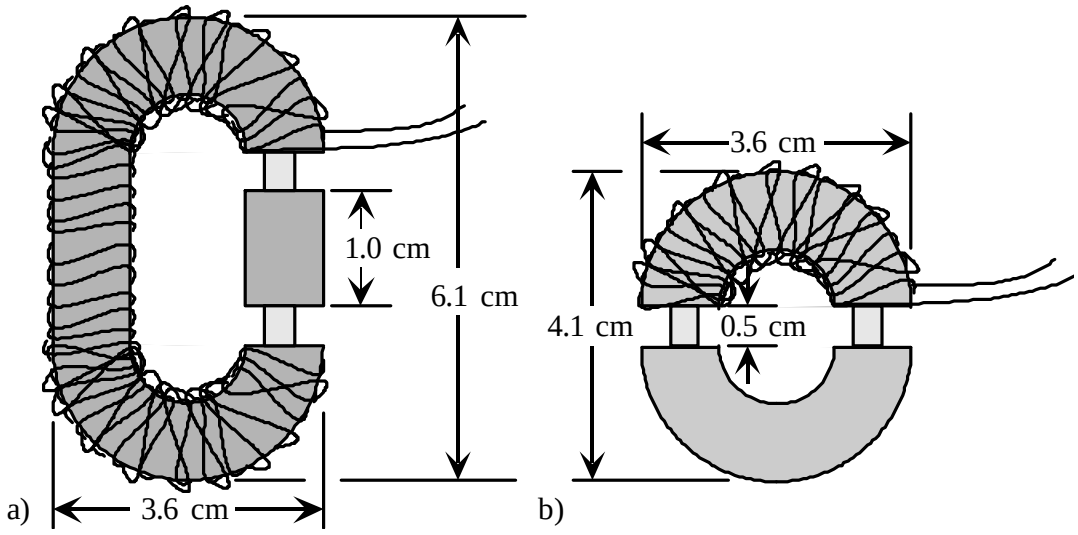

Figure 2.3: a) Longitudinal/shear and b) squeeze mode devices and their geometries.

The mass of the wire, M_{wire}, is a function of not only wire density, but also the number of turns of wire. The mass of the wire was approximated as $M_{wire} = \rho_{wire} N \left(\frac{d_{wire}^2 N}{2s} + 2s \right)$, where d_{wire} is the diameter of the wire, and ρ_{wire} is the density of the wire, in kg/m.

Figure 2.3 shows the final dimensions of the devices. The longitudinal and shear devices are actually the same device; the device is simply rotated 90°with respect to the direction of excitation in order to achieve shear and longitudinal excitation. Each device had 183 turns of magnet wire. The devices were designed by not only satisfying Equations 2.4, 2.5, 2.6, and 2.8, but also by adhering to the physical limitations of the power supply. The limitations of the power supply were that the current, $I < 6$A, and the power consumed was less than 200 W. The final design weight was 82 g for the squeeze mode device and 166 g for the longitudinal/shear device. Although the longitudinal/shear device exceeded the total mass permitted, excess mass was built into the system in order to interface with the experimental setup.

Figure 2.3 shows that MREs were selected such that $L = 5$ mm. The number of turns of wire was selected to be $N = 183$, and current levels were selected to be no more than $I = 4$ A. MREs were specified so that both MRE pieces in a device could be cured at the same time under identical curing conditions. For this reason, the MRE cross-sectional area is that of a semi-circle, with a radius of $r_{MRE} \approx 4$ mm. The following section describes

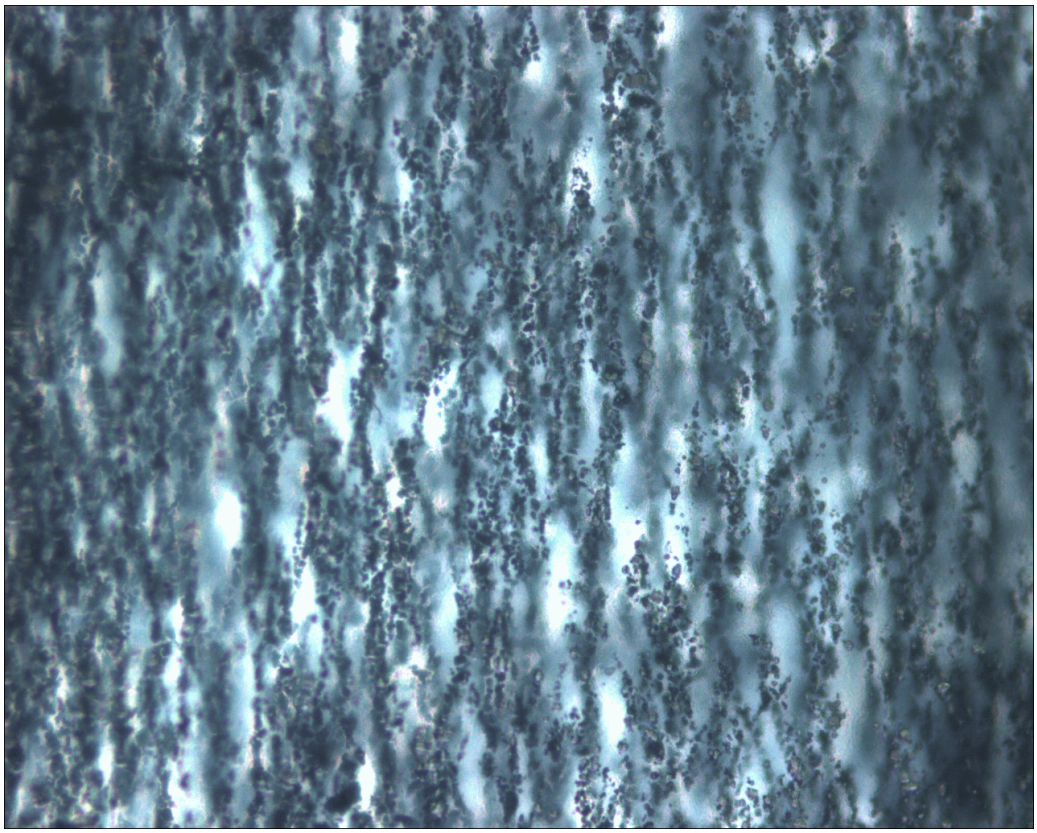

Figure 2.4: A 35% MRE, sliced, backlit, and magnified by a factor of 20.

the mold design that produced MREs containing aligned iron particles in this particular geometry.

2.2 Mold Design

A mold was constructed for two purposes; it functioned to hold elastomer-iron mixtures in the proper geometry until the MRE cured, and it provided the necessary magnetic field to align the MRE iron particles, as depicted in Figure 2.4. The MRE was embedded in methyl methacrylate, and sliced along the direction of the magnetic field to a thickness of 210 μm. The slice was then placed on a slide and polished. The MRE was backlit and magnified by a factor of 20. The black dots are in fact iron particles; this picture shows that the iron particles did in fact line up in chains when they were cured in the presence of a magnetic field.

Figure 2.5 shows an exploded view of the five mold pieces. The plunger, the cover,

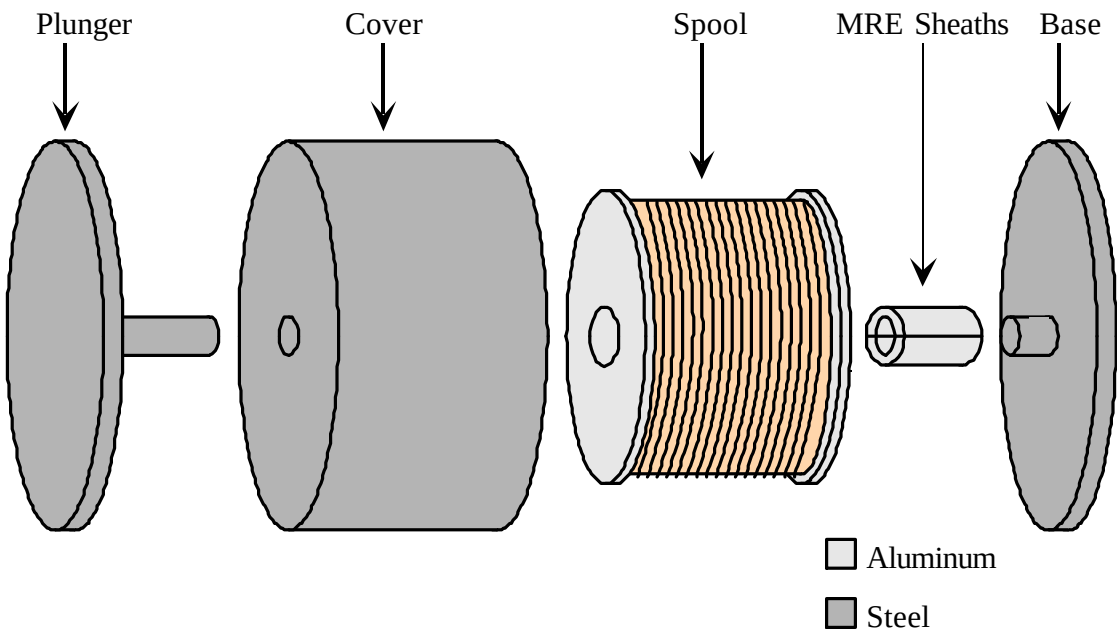

Figure 2.5: Exploded view of an MRE mold.

and the base were constructed from low-carbon steel, which facilitated a continuous flux path. The spool and the MRE sheaths, however, were constructed out of aluminum so that the magnetic path of least resistance would be through the MRE, and not through some alternative path through the mold. Approximately 900 turns of magnet wire were wrapped around the spool to ensure that the iron particles would be magnetically saturated during cure. Figure 2.6 shows a cross-sectional view of the mold. The five pieces work together to create a continuous flux path that traveled through the MRE; red arrows represent the flux paths.

2.3 Device Construction

This section describes the total device construction procedure, from MRE preparation to device assembly. The mold described in the preceding section was used to cure MREs. Before MREs can be cured, they must be properly mixed. After the cure is complete, the MREs must be secured to the devices.

Each of the MREs were constructed from RTV 6186, a two-part silicone gel manufactured by GE Silicone, and ISP grade R-1430 micro iron particles, which have an average

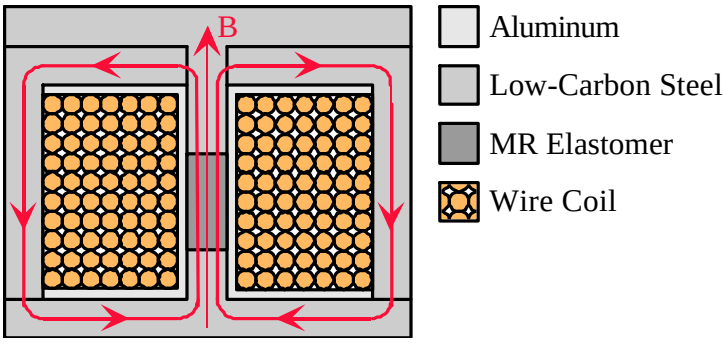

Figure 2.6: A cross-sectional view of the MRE mold and its components.

diameter of 6-9 microns. 3.0 g of silicone gel were used for each silicone cure; the appropriate mass of iron particles was calculated to yield a desired volume fraction of iron.

Early testing revealed that MREs containing less than 30% volume fraction of iron particles broke under the weight of the absorber mass. Since increasing the amount of particles in an elastomer composite increases ultimate strengths if the particle diameters are small[11], talc powder was added to yield a net 30% volume fraction of particulate matter. This was to ensure that the MRE would have adequate yield strength to support the weight of the absorber mass.

To properly make an MRE, the mold was first prepared by spraying all surfaces with Miller Stephenson 122D dry lubricant. Once the surfaces were dry, the mold was assembled such that it appeared as Figure 2.6, except that the plunger was left out. The mold coil wires were attached to the power supply. For this particular mold, the current source was used both to generate magnetic field as well as heat the mold, so an additional oven was not required. It is important to note that the mold was not preheated; preliminary tests revealed that some amounts of the MRE would cure upon contact if the mold was preheated, thus yielding a flawed part.

Once the mold was prepared, 1.5 g of part B silicone was poured into a glass beaker. The appropriate amount of iron and talc particulate matter was massed and added to the glass beaker. The mixture was stirred well, scraping the sides of the glass beaker, until the particulate and silicone was well mixed, for about a minute. 1.5 g of part A silicone was then added to the beaker. The mixture was then mixed vigorously for five minutes over low

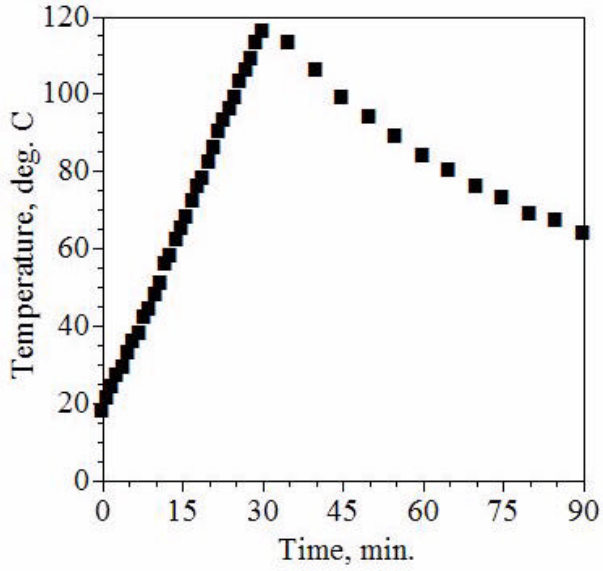

Figure 2.7: MRE temperature during and after cure.

heat of about 38°C. The mixture was poured into the mold, the plunger was put in place, and the power supply was turned on. The power supply remained on for thirty minutes, at which point the power was turned off, and the mold and MRE was allowed to cool.

The silicone used in the MRE needed to be heated to above 70°C for at least 30 minutes in order to cure, but not longer than 90 minutes. If an MRE cures for longer than 90 minutes above 70°C, then the MRE becomes much stiffer. Figure 2.7 shows the temperature profile of an MRE during cure as well as after the power supply has been shut off. It can be seen that the MRE is above 70°C for approximately 58 minutes.

Once an MRE had fully cooled to ambient room temperature, the mold was disassembled and the MRE was removed. The MRE was sliced lengthwise to create two identical springs with "D"-shaped cross-sectional MRE springs. The MRE springs were then connected to the base and absorber mass using Loctite 454 adhesive. The MRE springs were first attached to the absorber mass and allowed to cure for at least an hour. Then the MRE springs were attached to the base mass using the adhesive, again allowed to cure for at least an hour, but as much as twenty-four hours to achieve a full cure.

CHAPTER III

EXPERIMENTAL SETUP, RESULTS, AND DISCUSSION

The MREs described in Chapter 2 were assembled into a squeeze-mode vibration setup to find the iron content that generated the maximum natural frequency shift. MREs were cured with different iron content and named according to the total volume fraction that the iron took up in the MRE. Once the MRE with the maximum frequency shift in a squeeze-mode vibration absorber device was identified, that MRE was used to test all other vibration absorber devices and experimental conditions. These different devices were examined to determine the effect of different vibration absorber configurations on vibration absorber performance. Two mechanical properties were examined for each MRE recipe tested: the ratio of flux density through a MRE to the flux density through the base iron core, and the natural frequency change of each absorber in response to incremental magnetic field intensity increases through the electromagnet coil. Absorbers were examined for transient response to a step input change in magnetic field. The MRE with the largest frequency change in the squeeze mode device was placed into longitudinal and shear mode configurations to determine the effect of geometric constraints on MRE performance.

3.1 Experimental Setup

Once the devices were assembled according to the procedures described in Chapter 2, they were mounted on an experimental setup in order to test their physical properties. Figure 3.1 is a schematic of the setup used to obtain experimental results. A magnetic field was delivered by attaching the wire coil ends to a KEPCO model 36-6D power supply, which supplied up to 6 A of direct current. For experiments requiring device excitation, a data acquisition system was used to generate a white noise signal, low-pass filtered to 1000 Hz. This signal was amplified by an LDS PA25E power amplifier, and excited the base mass using an LDS V205 shaker. The shaker was rigidly attached to the base mass.

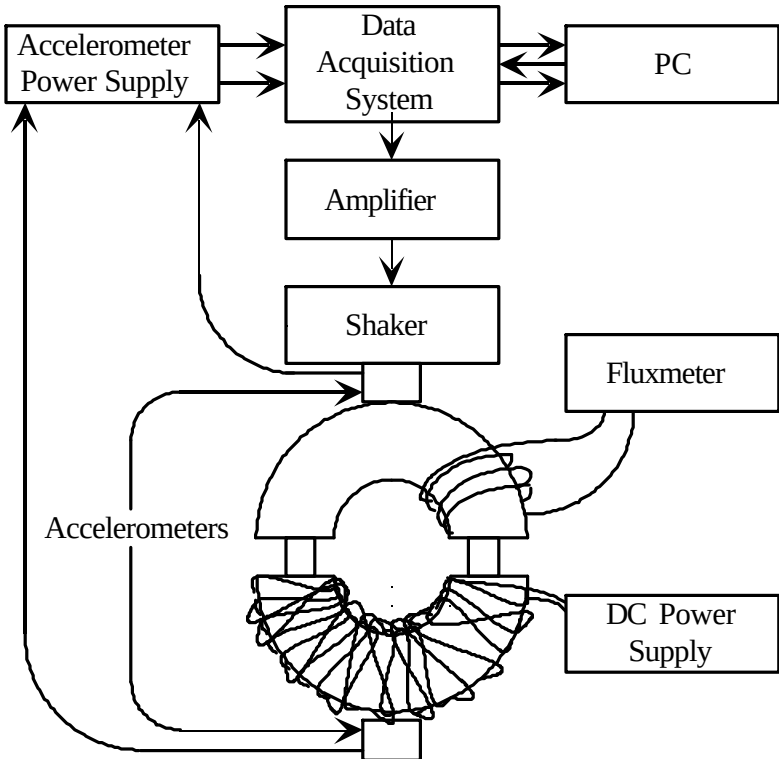

Figure 3.1: Schematic diagram of the experimental setup used to evaluate MRE properties.

Data in the form of magnetic field, displacement, and acceleration were collected to determine device characteristics. Magnetic fields were measured by a Lakeshore model 480 fluxmeter, using a sensor with 125 turns of wire. The fluxmeter probe could be placed around the base mass, as indicated by Figure 3.1, or around the MREs. Acceleration data was collected by a PCB 303A02 accelerometer, attached to the absorber mass, and a PCB 288A11 accelerometer, which was attached to the base mass. Information that was static in nature, such as the static displacement of the absorber mass, was measured using a Philtec model D100-QPT displacement probe. The displacement probe was located such that it could measure the absolute displacement of the absorber mass. Data from accelerometers and the displacement probe were acquired by a Siglab model 50-21 data acquisition system, and then transferred to a PC.

Figure 3.1 shows a generalized experimental setup. However, it is important to note that not all four measurement devices were used at all times. In the following sections, the results from the experimental work are presented. The specific equipment setup for each

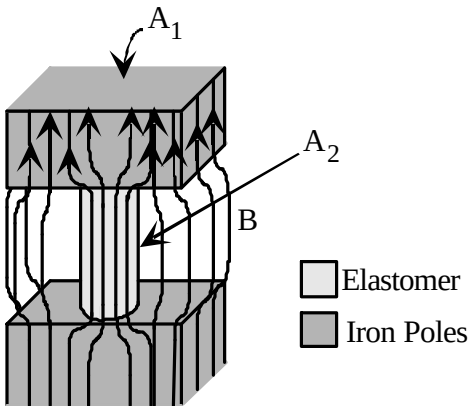

Figure 3.2: Flux lines through two materials with unlike cross-sectional areas.

experiment is explained, and then the results are discussed.

3.2 Flux Density Ratios

During the device design phase, discussed in the Chapter 2, it became clear that there was uncertainty concerning the predicted magnetic field through the MRE itself. Figure 3.2 shows theoretical flux lines as they travel through an absorber gap partially filled by an MRE. It was anticipated that some of the flux lines would pass outside the MRE, and some would concentrate and travel through the MRE. A flux density ratio was generated, such that

$$r = \frac{B_{MRE}}{B_{st}}, \tag{3.1}$$

where r is the flux density ratio, B_{MRE} is the flux density through an MRE, and B_{st} is the flux density through the absorber mass.

In order to determine flux density ratios, a magnetic field was generated using the coil around the absorber mass, starting with 0 kA/m, and increasing by increments of 2.3 kA/m until 18.3 kA/m was reached. For each field intensity level, flux density through the MRE was recorded. Once 18.3 kA/m was reached, a fluxmeter probe was connected around the base mass, and the same experiment was repeated, this time measuring the flux density through the base mass iron. Figure 3.3 shows sample data for this experiment, where an MRE with 35% iron content was tested. The data yielded a linear relationship. For the

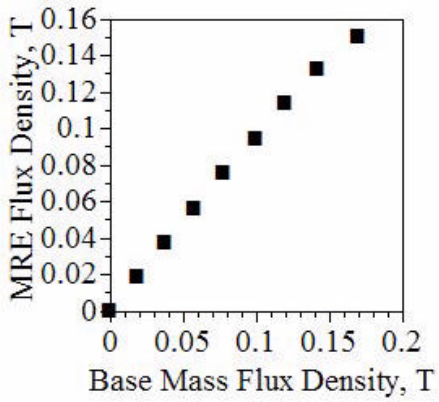

Figure 3.3: Flux density through the MRE versus through the base mass for a 35% MRE.

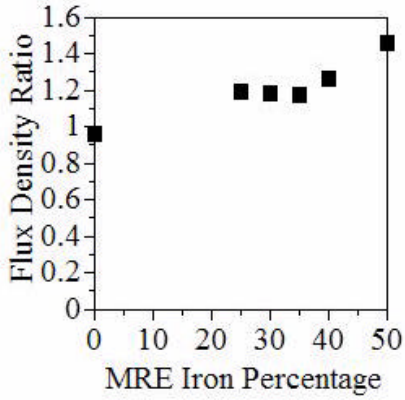

Figure 3.4: Flux density ratio for MREs with different iron content, by percent volume.

case of the sample data, a slope or flux density ratio of 1.17 was found, with an R^2-value of greater than 0.99.

Figure 3.4 shows the flux density ratios found for different MRE concentrations. A ratio of less than 1.0 indicates that there was net flux fringing around the MRE, and a ratio greater than 1.0 indicates that there was flux concentration through the MRE. All flux density ratios had R^2-values of at least 0.95. The results in Figure 3.4 show that for all MREs containing any finite amount of iron, there was net flux concentration. This means that the effect of having iron in the MRE caused enough flux concentration to counteract the net flux decrease associated with air gaps.

Although the results from Figure 3.4 indicate flux concentration occurs for any amount of iron in the MRE, this conclusion is drawn assuming that magnetic flux travels through

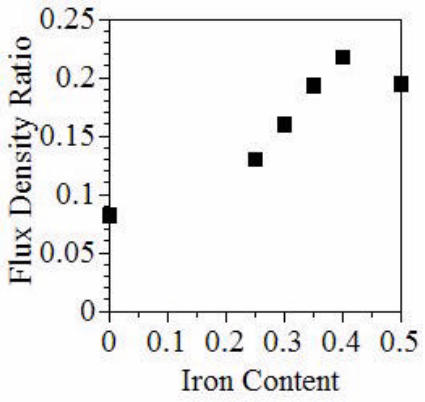

Figure 3.5: Ratio of flux density through MRE to flux density generated by coil for different MRE concentrations.

only one path. However, magnetic fields can travel through air, so the effect of multiple magnetic field paths must be considered. The ratio of the MRE flux density to the flux density emitted from the magnet coil can be seen in Figure 3.5. The flux density produced from the magnet coil can be determined by

$$B_{coil} = \frac{NI}{l}. \tag{3.2}$$

Figure 3.5 shows that 40% MREs yield the largest flux density ratios, retaining about 22% of the source flux density, whereas 0% MREs yield the smallest flux density, with less than 10% retention of flux density from the coil to the MRE. Figure 3.5 shows two trends; one trend indicates that the flux density ratio increases as the iron concentration increases. The other trend stems from the low flux density ratio numbers: the flux density through the MRE is 5 to 10 times lower than the flux density through the absorber mass. However, a different absorber geometry could help alleviate some of these problems; a larger air gap between the poles of the absorber mass could help limit the amount of flux circumventing the MREs.

3.3 MRE Frequency Change and Iron Content

The magnetic flux density described in the preceding section is important because it causes vibration absorber devices to change their natural frequency. The purpose of the work presented in this section was to quantify the natural frequency increase that MREs of

different iron content generate, and to find the iron content that generated the largest frequency increase in a squeeze mode device. After it was determined which iron content in an MRE generated the largest frequency increase, MREs with the same iron content were placed in longitudinal and shear mode devices, and the natural frequency for each of these devices was recorded as a function of magnetic field intensity.

MREs were placed in a squeeze mode vibration absorber configuration and the base mass was subjected to white noise, band limited at 1000 Hz. Acceleration data was collected from the base mass and the absorber mass. The MRE was modeled as a spring with complex stiffness, having a loss factor δ and stiffness K. The equation of motion governing the system was assumed to be

$$M\ddot{x}_{abs} + Ke^{i\delta}x_{abs} = Ke^{i\delta}x_{base}, \tag{3.3}$$

where M is the absorber mass, . An FFT was applied to the data, yielding a transfer function

$$H(\omega) = \frac{X_{abs}(\omega)}{X_{base}(\omega)} = \frac{Ke^{i\delta}}{Ke^{i\delta} - \omega^2 M} = \frac{\omega_n^4 - \omega^2\omega_n^2\cos\delta - i\omega^2\omega_n^2\sin\delta}{\omega_n^4 + \omega^4 - 2\omega^2\omega_n^2\cos\delta}, \tag{3.4}$$

where $\omega_n^2 = \frac{K}{M}$. The phase angle and amplitude of Equation 3.4 were found and analyzed to empirically determine the values of ω_n and δ for each data set. The phase angle between the absorber and base masses may be written as

$$\angle H(\omega) = \tan^{-1}\left(\frac{\omega^2\sin\delta}{\omega^2\sin\delta - \omega_n^2}\right). \tag{3.5}$$

Using Equation 3.5, the phase angle can be shown to cross -90° when

$$\omega = \omega_{90^\circ} = \frac{\omega_n}{\sqrt{\cos\delta}}. \tag{3.6}$$

Substituting this into Equation 3.4, the amplitude can be found to be

$$|H(\omega)| = \frac{\omega_{90^\circ}^2\cos\delta}{\left[\omega^4 + \omega_{90^\circ}^4\cos^2\delta - 2\omega^2\omega_{90^\circ}^2\cos\delta\right]^{1/2}}. \tag{3.7}$$

The natural frequency, ω_n, and loss factor, δ, were found by first identifying ω_{90° from the phase angle data. Amplitude data was calculated using Equation 3.7, where $\delta = \frac{n\pi}{40}$,

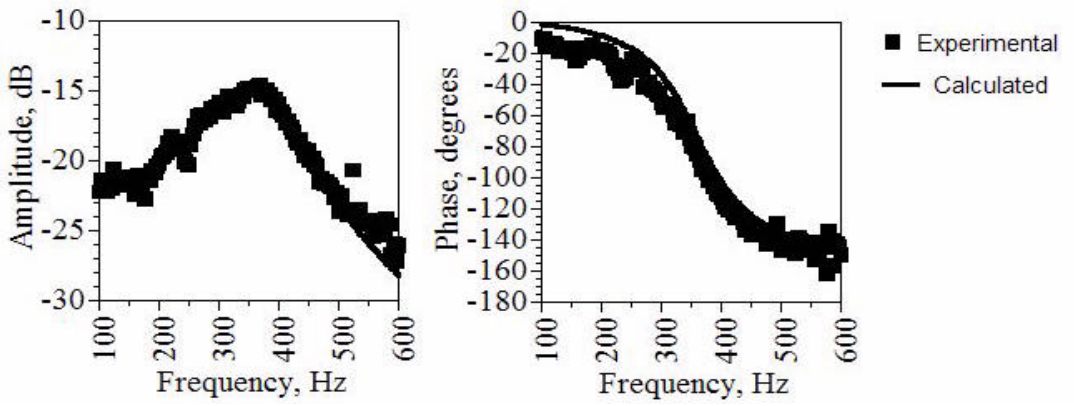

Figure 3.6: Experimental data from a 35% MRE was fit to elastomeric behavior where $\omega_n = 377$ Hz and $\phi = 0.432$ rad.

$n = 1, 2, \ldots 20$. The δ value was selected when

$$\frac{\partial\left(e^2\right)}{\partial\delta} = 2e\frac{\partial e}{\partial\delta} = 2\sum_{m=1}^{M}\left[\left(|y\left(\omega_m\right)| - |H\left(\omega_m, \delta_n\right)|\right)\cdot\left(-\frac{\partial\left|H\left(\omega_m, \delta_n\right)\right|}{\partial\delta_n}\right)\right] = 0, \tag{3.8}$$

where $y\left(\omega_m\right)$ is the experimental data value at frequency ω_m. Equation 3.8 finds the point of zero-slope in the squared-error curve. This indicated points of maximum and minimum error. Since

$$\frac{\partial\left|H\left(\omega, \delta\right)\right|}{\partial\delta} = \frac{-\omega_{90^\circ}^2\omega^4\sin\delta}{\left[\omega^4 + -\omega_{90^\circ}^4\cos^2\delta - 2\omega_{90^\circ}^2\omega^2\cos\delta\right]^{3/2}}, \tag{3.9}$$

values at $\delta = 0$ were ignored. Once a δ-value had been ascertained, the natural frequency, ω_n, was determined by substituting δ back into Equation 3.6. Amplitude and phase angle data is presented in Figure 3.6 for a 35% MRE; its natural frequency and loss factor were calculated to be $\omega_n = 377$ Hz and $\delta = 0.432$, respectively, using Equations 3.6 and 3.7.

Using this data fitting technique, natural frequency data for absorbers were recorded at 2.3 kA/m field intensity level intervals from 0 to 18.3 kA/m. Figure 3.7 shows a plot of average natural frequencies for each MRE at 0 kA/m, with error bars indicating the standard deviation in the samples. The 0 kA/m natural frequency increases as a function of iron content for MREs containing at least 30% iron. As mentioned in Chapter 2, MREs containing less than 30% iron by volume had talc powder added so that 30% of the overall MRE volume consisted of particulate matter. The increase in 0 kA/m natural frequency above iron contents of 30% is expected, then, as increasing iron content above 30% increases

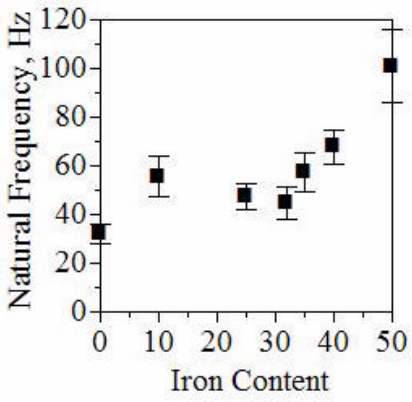

Figure 3.7: Natural frequencies for squeeze mode absorbers containing different MREs at 0 A current. Error shows +/- one s.d.

the base natural frequency. The natural frequencies below 30% would be expected to be constant, and while that is roughly the case between 10% and 25%, the 0% iron is clearly significantly lower in natural frequency than any other MRE. One reason for this discrepancy between expectation and outcome could be explained by the difference between the talc powder and the iron powder; while a concerted effort was made to find an inert powder close in size to the iron, the talc powder particles were smaller than the iron particles. This means that to make up the same volume, the elastomeric matrix must spread around more particulate surface area, which could change the results. It has also been found that particulate matter composition within an elastomer does in fact affect the composite material's moduli.

Figure 3.8 shows the natural frequencies of each MRE at each field intensity level, normalized by the natural frequency at 0 kA/m, for each MRE iron content. The 35% MRE starts exhibiting an increased natural frequency at 6.9 kA/m, and has the largest frequency increase of the MREs examined. The other MREs appear to maintain constant natural frequencies through 13.8 kA/m, and all but the 0% MRE exhibit increased natural frequencies for 16.1 and 18.3 kA/m. The 0% MRE, on the other hand, does not increase, and in fact exhibits a 14% decrease in natural frequency response. This result, while somewhat surprising, is statistically significant according to Student's t-test, $0.05 < \alpha < 0.10$. The decrease in natural frequency actually matches with some basic magnetic theory that states

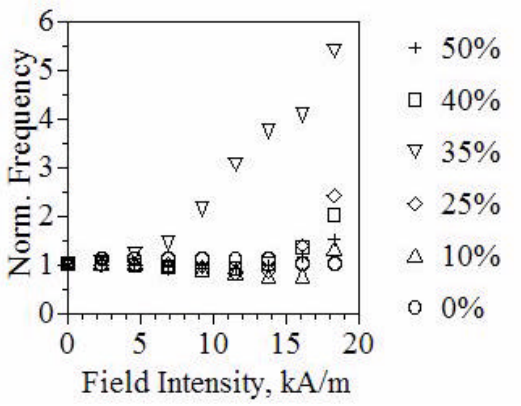

Figure 3.8: Natural frequencies at different current levels for MRE concentrations.

that

$$F_m = \frac{\alpha}{r^2}, \tag{3.10}$$

where F_m is the attractive magnetic force, α is a field strength-dependant constant, and r is the distance of separation between two fully saturated particles. The two saturated particles are the base and absorber masses when considering a 0% MRE placed in a vibration absorber configuration. When this attractive force interacts with the dynamic system, the equation of motion becomes

$$M\ddot{x}_{abs} + K^* x_{abs} = K^* x_{base} + F_m - Mg, \tag{3.11}$$

where $r = l_{eq} + x_{abs} - x_{base}$ is the distance of separation between the base and the absorber masses. The magnetic force can be linearized about l_{eq} using a Taylor series expansion and dropping higher order terms. This yields

$$M\ddot{x}_{abs} + \left(K^* - \frac{2\alpha}{l_{eq}^3}\right) x_{abs} = \left(K^* - \frac{2\alpha}{l_{eq}^3}\right) x_{base} + \frac{\alpha}{l_{eq}^2} - Mg. \tag{3.12}$$

Equation 3.12 shows that $K_{eq} = K^* - \frac{2\alpha}{l_{eq}^3}$, which means that K_{eq} decreases with increasing magnetic field and decreasing equilibrium spring length for a 0% MRE in an absorber configuration.

Figure 3.9 shows loss factor and natural frequency data for a 35% MRE at each field intensity level tested. While there are moderate frequency increases between 0 and 6.9

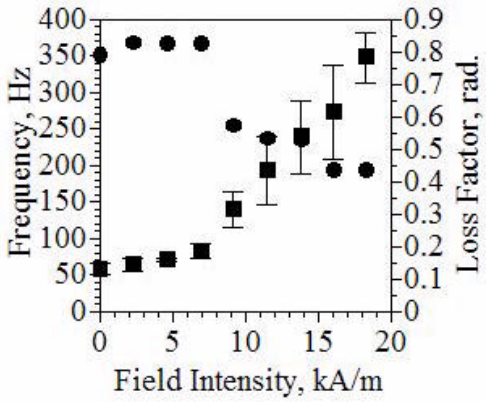

Figure 3.9: Frequency and loss factor response for a 35% MRE in squeeze mode.

kA/m, the large frequency increases start at about 9 kA/m. The loss factor, on the other hand, appears to be steady at roughly 0.8 radians below 9 kA/m, but then drops to about 0.6 radians, and continues to decrease to 0.4 radians between 9 and 18.3 kA/m. It should be noted that the loss factor data for the 35% MRE is not a typical response. In fact, there appears to be no typical pattern for loss factor data across the different iron concentrations. This could be due to the inherent errors associated with minimum squared error methodologies, and exacerbated by any errors in estimating the natural frequency.

Despite reservations regarding the accuracy of the computed loss factors, the average loss factor values for the MREs at each magnetic field level were used to calculate Q-values. Figure 3.10 shows the loss values of each MRE. Holdhusen and Cunefare found that damping values of 0.27-0.42 yielded optimal SSA performance [20]. The damping values found for good SSA performance translate to Q-values of 0.84-1.68. The MREs examined in this work are able to perform within this optimal Q-value range.

While Figure 3.8 and Figure 3.9 shows the vibration absorber's behavior at each field intensity level, there is interest in knowing what fractional increase can be expected between the no-flux state and the maximum-flux state. Rearranging the data presented in Figure 3.8, Figure 3.11 shows the net natural frequency increase between 0 kA/m and 18.3 kA/m. For each MRE the net fraction frequency change was calculated as

$$r = \frac{\omega_{\max} - \omega_{\min}}{\omega_{\min}}, \tag{3.13}$$

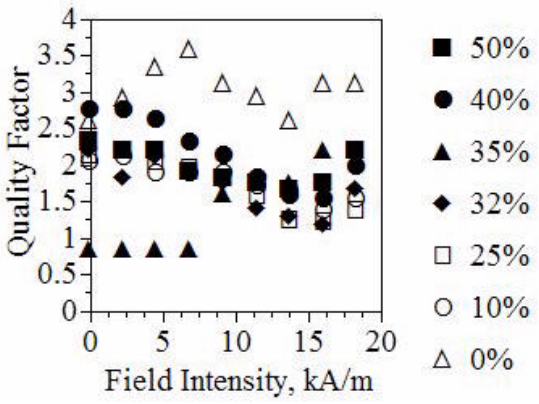

Figure 3.10: Quality factor for MREs of different composition.

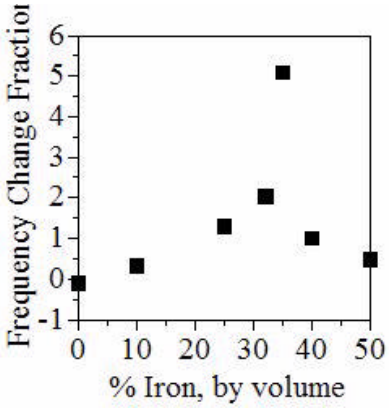

Figure 3.11: Natural frequency ratios for various MREs.

where ω_{max} and ω_{min} are the natural frequencies at 18.3 and 0 kA/m, respectively. It is clear that the 35% MRE yielded the largest frequency shift, an increase of approximately 510%. These results do not match up with the frequency shift predicted for a 27% iron as found by Davis [8]. However, the configurations used by Davis does not permit MREs to contract in the presence of a magnetic field; thus the prediction is not valid for this work.

By examining the flux density data presented in Figure 3.5, which shows that 35% and 50% MREs yield the largest flux density ratio between the absorber mass and the MRE, and the 0-kA/m natural frequency data from Figure 3.7, it is easy to explain why a 35% MRE performed the best. MREs containing less than 30% iron had roughly equivalent stiffnesses at 0 kA/m, but the flux density ratio through the MRE wasn't as high. Therefore these values would not be optimal. However, for MREs with 30% iron or above, there are

relatively high flux density ratios, but the 0 kA/m natural frequency increases as a result of increased particle density. This means that the MRE will exhibit optimal behavior when the flux density ratio is maximized while the natural frequency at 0 kA/m is as low as possible.

It is important to discuss the spring's equilibrium length, because that was observed to change as a function of magnetic field. Considering a 0% MRE placed in an absorber configuration, it is evident that there are only two iron pieces in the entire absorber: the base mass and the absorber mass. If one treats each of these masses as a "particle", a static analysis of Equation 3.12 yields

$$\left(K^* - 2\frac{\alpha}{l_{eq}^3}\right)\Delta = \frac{\alpha}{l_{eq}^2} - Mg, \tag{3.14}$$

where $\Delta = x_{abs} - x_{base}$ is the static change in equilibrium length from the zero-magnetic field static equilibrium length. This means that

$$\Delta = \frac{\left(\alpha - Mgl_{eq}^2\right) l_{eq}}{K^* l_{eq}^3 - 2\alpha}. \tag{3.15}$$

The above analysis is only valid when describing attraction of two magnetic particles, or a 0% MRE in a vibration absorber configuration, and does not describe in any way the natural frequency changes experienced by any MREs with a finite amount of iron particulate matter. The analysis conducted on 0% MREs indicate that whatever the stiffness-change mechanism, it is more than likely tied to a 0th-order equilibrium length change. Based on this presumption, the absorber mass's static displacement was measured as a function of time to determine the transient characteristics of the stiffness changes in MREs.

3.4 MRE Transient Behavior in Squeeze Mode

As discussed previously, a link has been established between static displacement and stiffness change for 0% MREs. While the analysis is not valid for any MREs with finite amounts of iron particles, it is reasonable to assume that the time it takes for an MRE to undergo its static deformation would in some way correlate to the time it takes for an MRE to change its stiffness. Since there is no way to measure stiffness instantaneously, static displacement

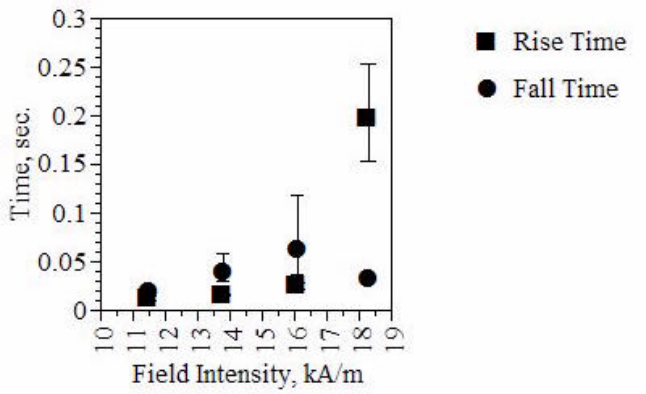

Figure 3.12: Rise and fall times for a 35% MRE.

was measured as at least an indication of the transient time present in MREs excited in squeeze mode.

Since 35% MREs were found to generate the largest frequency increase, a 35% MRE was placed in squeeze mode to examine its transient properties. The device was suspended as shown in Figure 3.1, and measurements were recorded from the displacement probe and the flux density probe around the base mass. The device was not excited, but a square wave with a period of 2 seconds was generated by the data acquisition system and supplied to the power supply for the wire coil.

Figure 3.12 shows the rise time and drop time, as well as their ranges, for a 35% MRE in squeeze mode when field intensity is switched on or off. Rise and drop times were defined as the time the absorber mass required to travel between 5% and 95% of the static displacement. This rise and drop time includes the response time of the power supply, the response of the coil itself to the current, and then the time it takes for the physical system to rise or drop. Figure 3.12 shows that the fall time is slower from 11.6 to 16.1 kA/m; at 18.3 kA/m the rise time is significantly longer than the fall time.

Figure 3.13 shows one period response for the device when a 18.3 kA/m square wave was supplied. There is a noticeable gap in rise time between the flux density and the displacement. The physical device parameters clearly contribute to a long, overdamped system response. The discrepancies in rise and drop time characteristics indicate that external forces, such as gravity, play a significant role in transient response.

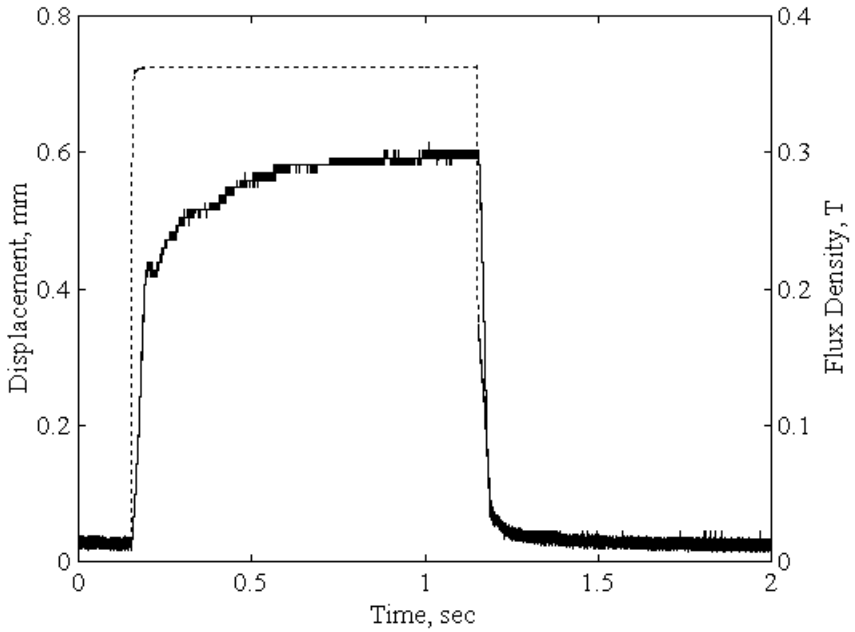

Figure 3.13: Transient responses of a 35% MRE in squeeze, excited by a 18.3 kA/m square wave. - - displacement, – flux density.

Figure 3.14 shows a small time window around the current drop from Figure 3.13. Although the field intensity drop was a near-instantaneous drop, it appears that the flux density only drops about halfway before slowing its descent. Overall, the flux drop was found to be approximately 0.03 s.

Data from Figure 3.13 and Figure 3.14 indicate that the transient response of 35% MREs in shear configuration are slower than desired. However, the data was in response to a step increase and decrease; from this data, future empirical equations can be developed and future inputs can be shaped to result in optimal transient responses.

3.5 Natural Frequency Response to Longitudinal, Shear, and Squeeze Mode Devices

Natural frequency data for longitudinal and shear devices were measured in the same way that natural frequency data was measured from the squeeze mode device, presented in Section 3.2. 35% MREs were placed in longitudinal and shear devices and tested for natural frequency responses. Figure 3.15 presents natural frequency data, normalized to the natural

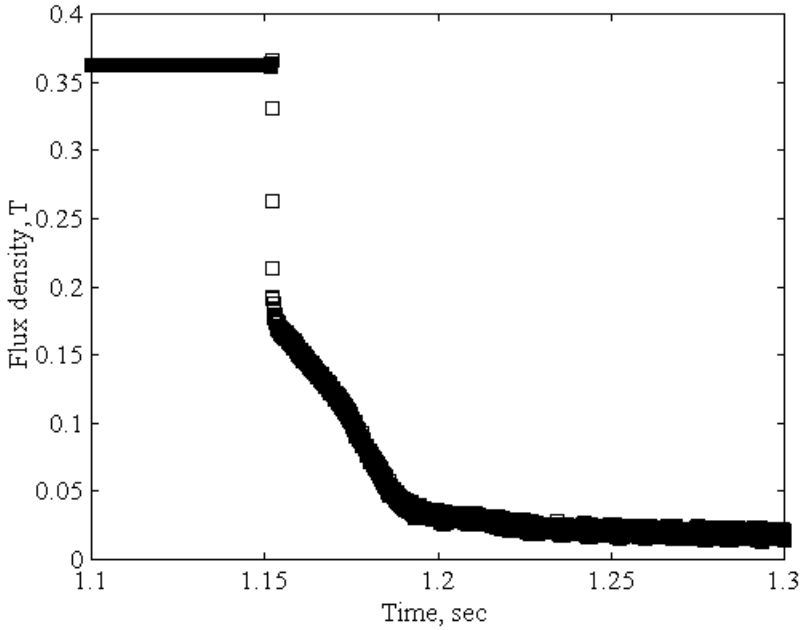

Figure 3.14: Flux drop for a 35% MRE experiencing an 18.3 kA/m to 0 kA/m step change.

frequency at 0 kA/m for each respective device. The squeeze mode device experienced the largest frequency shift, with a frequency range of 57-347 Hz and a 510% frequency increase. The longitudinal device also experienced a large shift, with an operation frequency range of 78-449 Hz and a 473% increase. The shear mode device experienced the smallest frequency increase, although it was still a 183% increase, operating in the 26-74 Hz range.

From Figure 3.15, it is clear that the longitudinal and squeeze mode devices experienced the largest frequency change. In examining the longitudinal and squeeze mode responses, it appears that although these two devices experienced similar natural frequency increases, the squeeze mode device may have potential to further increase its natural frequency at current levels above 18.3 kA/m. The difference in frequency responses of the longitudinal MRE at 16.1 kA/m and 18.3 kA/m were statistically insignificant, indicated that the particulate matter within the MRE were magnetically saturated.

Another explanation of the responses of the longitudinal and shear mode devices lies in geometric limitations. The longitudinal device had a fixed gap of 1 cm, which held the iron particles close together. The squeeze mode device instead allowed the device to have a total

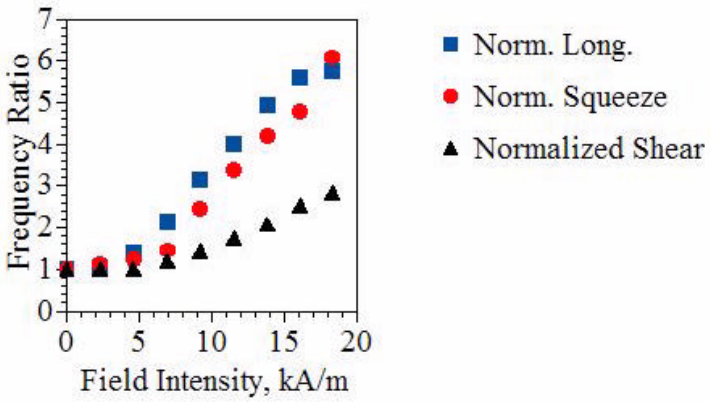

Figure 3.15: Squeeze, shear, and longitudinal mode device normalized natural frequency response for a 35% MRE.

gap of 1.3 cm, which meant that the iron particles were stretched apart. This means that a magnetic field would need to be applied to cause the squeeze mode device gap to decrease to 1 cm. However, the squeeze mode device has the capability to decrease the total gap to less than 1 cm, which means that the squeeze mode device should be able to exhibit a larger frequency change.

Whereas exciting MREs parallel to the direction of magnetic flux yielded very large frequency changes, exciting the MRE in shear has a much smaller, although significant, frequency increase. The shear device experienced a 183% increase in natural frequency. Davis developed an equation that predicts the maximum shear modulus, as detailed in Equation 1.2 [8]. Since $\omega_n^2 = GA/(LM)$, Equation 1.2 can be rewritten so that

$$\frac{\Delta G_{\max}}{G(0)} = r(r+2), \tag{3.16}$$

where r is the fraction of natural frequency increase. A 700% increase in stiffness can be found when Equation 3.16 is applied to the data acquired in this research. Davis had predicted a maximum stiffness change of only 171%, much lower than what was found here. However, the elastomer used here was significantly softer than that used by Davis, so the assumption of zero contractions is not valid in this case.

CHAPTER IV

CONCLUSIONS

MREs were selected to be used as tunable springs in three vibration absorber devices. The vibration absorbers were developed with the overall goals of weighing less than 100 g, being no longer than 5 cm in any direction, and having an operational natural frequency of less than 100 Hz. The main purpose of these devices was to have a controllably variable natural frequency. An MRE was chosen as a variable stiffness spring in these devices because MREs have variable stiffness moduli in the presence of magnetic fields, a wide range of baseline stiffnesses, and a large natural frequency change in the presence of magnetic fields. Furthermore, magnetic fields pose little risk and are low-power devices.

MREs were designed to fit within three absorbers. One device excited the MRE in squeeze mode, one in longitudinal mode, and one in shear mode. MREs tested in squeeze mode demonstrated that MREs containing 35% iron particles by volume yielded maximum frequency shifts, achieving a 510% frequency increase over a frequency range of 57-347 Hz for the specific devices. 35% MREs also exhibited the one of the largest flux density ratios between the MRE and the base mass, and the smallest baseline natural frequency of the MREs that exhibited large flux density ratios.

35% iron fraction MRE performance was compared across the squeeze, longitudinal, and shear mode devices. Squeeze mode devices exhibited the largest frequency shift, followed closely by the longitudinal mode device with a 473% increase and an operational frequency of 78-449 Hz. Although the squeeze and longitudinal mode devices had similar natural frequency increases, the longitudinal mode device exhibited signs of magnetic saturation within the MRE. The natural frequency was not significantly different between 16.1 kA/m and 18.3 kA/m, which indicates that continuing to add field intensity would not increase performance. However, the squeeze mode device had not saturated, which means that the squeeze mode device potentially could have an even larger natural frequency increase than

what was presented here.

Both longitudinal and squeeze mode devices performed significantly better than the shear mode device. This indicates that whatever the geometric setup, natural frequency increases are maximized by exciting devices parallel to the direction of magnetic field. The shear mode device exhibited a 183% increase, operating in the 26-74 Hz range. While this increase is significantly larger than predicted by Davis [8], the elastomeric substrate used to create the MREs for this work was also significantly softer than the synthetic rubbers considered by Davis in his work, and thus allowed for contractions.

MREs excited in squeeze mode were observed to visibly contract when subjected to large magnetic fields, or field intensitys of at least 11.6 kA/m. Since there is no way of instantaneously measuring frequency, the static displacement of these MREs in squeeze was presumed to correlate in some way to the frequency increase. Measurements indicated that the rise and fall times are sensitive to outside forces, such as gravity, and are slower than desired.

REFERENCES

[1] "Magnetic circuit design," *Lord Corporation, Magnetics Division*, 2001.

[2] Abe, M. and Igusa, T., "Semi-active dynamic vibration absorbers for controlling transient response," *Journal of Sound and Vibration*, vol. 198, no. 5, pp. 547–569, 1996.

[3] Bossis, G., Abbo, C., Cutillas, S., Lacis, S., and Metayer, C., "Electroactive and electrostructured elastomers," in *Proceedings of the 7th International Conference on Electro-Rheological Fluids and Magneto-Rheological Suspensions* (Tao, R., ed.), (Honolulu, Hawaii), pp. 18–27, World Scientific Press, 1999.

[4] Corr, L., R. and Clark, W. W., "Piezoceramic springs for structural semi-active multi-modal vibration control," in *Proceedings of the ASME Design Engineering Technical Conference*, vol. v 6 B of *18th Biennial Conference on Mechanical Vibration and Noise*, (Pittsburgh, PA United States), pp. 1343–1351, American Soceity of Mechanical Engineers, 2001.

[5] Cunefare, K. A., "State-switched absorber for vibration control of point-excited beams," in *ASME International Mechanical Engineering Conference and Exposition*, (Orlando, FL), 2000.

[6] Cunefare, K. A., DeRosa, S., Sadegh, N., and Larson, G., "State-switched absorber for semi-active structural control," *Journal of Intelligent Material Systems and Structures*, vol. 11, no. 4, pp. 300–310, 2000.

[7] Davis, C. L., Lesieutre, G. A., and Dosch, J., "A tunable electrically shunted piezoceramic vibration absorber," *SPIE*, vol. 3045, pp. 51–59, 1997.

[8] Davis, L. C., "Model of magnetorheological elastomers," *Journal of Applied Physics*, vol. 85, no. 6, pp. 3348–3351, 1999.

[9] Den Hartog, J. P., *Mechanical Vibrations*. New York: reprinted by Dover, 1956.

[10] Dosch, J., Lesiutre, G., Koopmann, G., and Davis, C., "Inertial piezoceramic actuators for smart structures," *SPIE*, vol. 2447, pp. 14–25, 1995.

[11] Drozdov, A. D. and Dorfmann, A., "The stress-strain response and ultimate strength of filled elastomers," *Computational Materials Science*, vol. 21, no. 3, pp. 395–417, 2001.

[12] Farshad, M. and Benine, A., "Magnetoactive elastomer composites," *Polymer Testing*, vol. 23, no. 3, pp. 347–353, 2004.

[13] Frahm, H., "Device for damping vibration of bodies," April 18 1911.

[14] Gavin, H. P., "Design method for high-force electrorheological dampers," *Smart Materials and Structures*, vol. 7, no. 5, pp. 664–673, 1998.

[15] Gavin, H. P., Hanson, R. D., and Filisko, F. E., "Electrorheological dampers part 1: analysis and design," *Journal of Applied Mechanics*, vol. 63, pp. 669–675, 1996.

[16] Ginder, J. M., "Rheology controlled by magnetic fields," in *Encyclopedia of applied physics* (Trigg, G. L., Vera, E. S., and Greulich, W., eds.), vol. 16, pp. 487–503, New York, NY: VCH Publishers, 1991.

[17] Ginder, J. M., Davis, L. C., and Elie, L. D., "Rheology of magnetorheological fluids: models and measurements technology," *International Journal of Modern Physics B*, vol. 10, no. 23-24, pp. 3293–3303, 1996.

[18] Ginder, J. M., Nichols, M. E., Elie, L. D., and Tardiff, J. L., "Magnetorheological elastomers: properties and applications," in *SPIE Conference on Smart Materials Technologies*, vol. 3675, (Newport Beach, CA), pp. 131–138, 1999.

[19] Guth, E., "Theory of filler reinforcement," *Journal of Applied Physics*, vol. 16, no. 20, pp. 20–25, 1945.

[20] Holdhusen, M. and Cunefare, K. A., "Damping effects on the state-switched absorber used for vibration suppression," *Journal of Intelligent Material Systems and Structures*, vol. 14, no. 9, pp. 551–561, 2003.

[21] Jolly, M. R., Carlson, J. D., Munoz, B. C., and Bullions, T. A., "The magnetoviscoelastic response of elastomer composites consisting of ferrous particles embedded in a polymer matrix," *Journal of Intelligent Material Systems and Structures*, vol. 7, no. November, pp. 613–622, 1996.

[22] Karnopp, D., Crosby, M. J., and Harwood, R. A., "Vibration control using semi-active force generators," *Journal of Engineering for Industry*, vol. 96, no. series B, no.2, pp. 619–626, 1974.

[23] Karnopp, D. C., "Active and passive isolation of random vibration," in *Isolation of Mechanical Vibration, Impact, and Noise* (Snowdon, J. C., ed.), vol. 1 of *ASME Applied Mechanics Division Serials*, pp. 64–86, New York, NY: ASME, 1973.

[24] Meinecke, E. A. and Taftaf, M. I., "Effect of carbon black on the mechanical properties of elastomers," *Rubber Chemistry and Technology*, vol. 61, no. 3, pp. 534–547, 1988.

[25] Meirovitch, L., *Elements of vibration analysis*. New York: McGraw Hill, 2nd ed., 1986.

[26] Morison, J. and Karnopp, D., "Comparison of optimized active and passive vibration absorbers," *American Automatic Control Council*, vol. 35, no. 2, pp. 932–938, 1973.

[27] Nichols, M. E., Ginder, J. M., Elie, L. D., and Pett, R. A., "Electrorheological elastomers useful as variable stiffness articles," October 5 1994.

[28] Rabinow, J., "Magnetic fluid torque and force transmitting device," Nov. 20 1951.

[29] Shiga, T., Okada, A., and Kurauchi, T., "Magnetroviscoelastic behavior of composite gels," *Journal of Applied Polymer Science*, vol. 58, no. 4, pp. 787–792, 1995.

[30] Sun, J. Q., Jolly, M., and Norris, M., "Passive, adaptive, and active tuned vibration absorbers-a survey," *Journal of Vibration and Acoustics*, vol. 177, no. 3B, pp. 234–42, 1995.

[31] Tang, J. and Wang, K. W., "Vibration control of rotationally periodic structures using passive piezoelectric shunt networks and active compensation," *Journal of Vibration and Acoustics*, vol. 121, pp. 379–390, 1999.

[32] Watson, J. R., "Method and apparatus for varying the stiffness of a suspension bushing," March 11,1997 1997.

[33] Zhou, G. Y., "Shear properties of a magnetorheological elastomer," *Smart Materials and Structures*, vol. 12, pp. 139–146, 2003.